Semiautomated Confocal Imaging of Fungal Pathogenesis on Plants: Microscopic Analysis of Macroscopic Specimens

KATHARINE R. MINKER,[1] MEREDITH L. BIEDRZYCKI,[2] ABHISHEK KOLAGUNDA,[2,3] STEPHEN RHEIN,[2,3] FABIANO J. PERINA,[2] SAMUEL S. JACOBS,[4] MICHAEL MOORE,[4] TIFFANY M. JAMANN,[5] QIN YANG,[6] REBECCA NELSON,[7] PETER BALINT-KURTI,[6,8] CHANDRA KAMBHAMETTU,[3] RANDALL J. WISSER,[2]* AND JEFFREY L. CAPLAN[1,4]*

[1]*Department of Biological Sciences, University of Delaware, Newark, Delaware 19716*
[2]*Department of Plant and Soil Sciences, University of Delaware, Newark, Delaware 19716*
[3]*Department of Computer and Information Sciences, University of Delaware, Newark, Delaware 19716*
[4]*Department of Bio-Imaging Center, Delaware Biotechnology Institute, University of Delaware, Newark, Delaware 19711*
[5]*Department of Crop Sciences, University of Illinois at Urbana-Champaign, Urbana, Illinois 61801*
[6]*Department of Plant Pathology, North Carolina State University, Raleigh, North Carolina 27695*
[7]*School of Integrative Plant Science, Cornell University, Ithaca, New York 14853*
[8]*USDA-ARS, Plant Science Research Unit, Raleigh, North Carolina 27695*

KEY WORDS plant–pathogen interactions; disease resistance; confocal microscopy; tissue clearing; image analysis

ABSTRACT The study of phenotypic variation in plant pathogenesis provides fundamental information about the nature of disease resistance. Cellular mechanisms that alter pathogenesis can be elucidated with confocal microscopy; however, systematic phenotyping platforms—from sample processing to image analysis—to investigate this do not exist. We have developed a platform for 3D phenotyping of cellular features underlying variation in disease development by fluorescence-specific resolution of host and pathogen interactions across time (4D). A confocal microscopy phenotyping platform compatible with different maize–fungal pathosystems (fungi: *Setosphaeria turcica*, *Cochliobolus heterostrophus*, and *Cercospora zeae-maydis*) was developed. Protocols and techniques were standardized for sample fixation, optical clearing, species-specific combinatorial fluorescence staining, multisample imaging, and image processing for investigation at the macroscale. The sample preparation methods presented here overcome challenges to fluorescence imaging such as specimen thickness and topography as well as physiological characteristics of the samples such as tissue autofluorescence and presence of cuticle. The resulting imaging techniques provide interesting qualitative and quantitative information not possible with conventional light or electron 2D imaging. *Microsc. Res. Tech. 00:000–000, 2016.*

INTRODUCTION

Our understanding of natural variation is defined by what we measure and how we measure it. Features and phenomena occurring at microscopic levels are manifested as macroscopic phenotypes. Thus, the availability of methods for microscopy on multiple samples and across macroscopic scales is critical to advancing organismal and comparative biology. For research on host–pathogen interactions, which was the context for this study, understanding how different host and pathogen genotypes alter the progression of pathogenesis can shed light on the nature of disease resistance. Therefore, we have developed a multisample, macrospace, and microscopic imaging platform to study pathogenesis of three fungal pathogens of maize, *S. turcica*, *Cochliobolus heterostrophus*, and *Cercospora zeae-maydis*. Although the methods and examples described here have been developed as part of a study focused on examining plant–pathogen interactions, their application is not limited to that study and a broad range of applications are readily conceivable.

Despite the potential benefits of studying microscopic phenotypes, a number of challenges exist, particularly to characterize quantitatively varying interactions at a microscopic level. Capturing a small

Additional Supporting Information may be found in the online version of this article.

*Correspondence to: Randall J. Wisser, Department of Plant and Soil Sciences, University of Delaware, 152 Townsend Hall, 531 South College Avenue, Newark, DE 19716 (or) Jeffrey L. Caplan, Delaware Biotechnology Institute, University of Delaware, 15 Innovation Way, Suite 117, Newark, DE 19711.
E-mail: jcaplan@udel.edu

Present address of Fabiano J. Perina: Cerrado Research Center, Brazilian Agricultural Research Corporation (Embrapa Algodao) C. Grande, PB 58428-095, Brazil.

Present address of Samuel S. Jacobs: Dogfish Head Craft Brewery, Inc., Milton, Delaware 19968, USA.

Received 29 October 2015; accepted in revised form 6 June 2016

REVIEW EDITOR: Dr. Mayandi Sivaguru

Katharine R. Minker and Meredith L. Biedrzycki contributed equally to this work.

Competing Interest: The authors declare that they have no competing interests.

Contract grant sponsor: U.S. NSF Plant Genome Program; Contract grant number: IOS-1127076.

DOI 10.1002/jemt.22709
Published online 00 Month 2016 in Wiley Online Library (wileyonlinelibrary.com).

number of events, as is typical in microscopy studies, is not sufficient for the analysis of quantitative differences where statistical inference is required; imaging platforms that capture numerous, measurable events are needed. This demands a range of developments, including technology for rapid sample processing and imaging; a capacity to image specimens with multiple interaction events (e.g., millimeter-scale areas of a specimen in which micrometer-scale events occur); techniques that differentiate and resolve relevant features of the interaction (such as host versus pathogen and structures within each organism); computational methods to identify and measure phenotypes in image data; and a cyberinfrastructure environment to facilitate big data processing.

Some hurdles to resolving microscopic features have to some degree been overcome by advances in microscopy such as fluorescent laser scanning confocal and multiphoton imaging. These techniques have become increasingly popular as they confer the benefits of three-dimensional imaging (Buda et al., 2009; Sørensen et al., 2012). In contrast to conventional two-dimensional light or electron microscopy, three-dimensional laser scanning confocal microscopy allows for in situ investigation of structures without physically sectioning and can be used for the identification and quantification of features of a specimen (such as topography and thickness; Buda et al., 2009). Confocal and multiphoton microscopy techniques have also been enhanced through utilization of fluorescent probes. Fluorescent proteins, fluorescently labeled antibodies, and fluorescent stains allow for the differentiation of cellular and tissue structures making three-dimensional rendering and reconstruction of structures in specimens possible.

Although fluorescence imaging techniques have been widely applied to plant imaging, some challenges remain. One of these challenges is that depth of fluorescence imaging in plant material is often obstructed by light scattering molecules present in the cuticle, vasculature, and mesophyll tissues (Wuyts et al., 2010). Despite the fact that multiphoton imaging generally can penetrate deeper into tissue, clearing of these light scattering molecules is still necessary to achieve optimal and fully traverse imaging. Chemical clearing agents such as the traditionally used chloral hydrate and recently established Sca*l*eP (Warner et al., 2014) and other methods (Kurihara et al., 2015; Palmer et al., 2015; Wuyts et al., 2010) have been shown to increase transparency in plant tissue and improve three-dimensional imaging quality. The increase in imaging resolution of three-dimensional structures is especially valuable during the investigation of plant–pathogen interactions as spatiotemporal associations between organisms can be elucidated.

Here, we describe the components of a platform for semiautomated microscopic imaging and analysis of plant leaves infected with fungal pathogens. These methods can be adapted for microscopic analysis of different plant–microbe pathosystems, such as the three fungal pathogens of maize demonstrated here, and plants in general. We anticipate that some of these developments will be found as useful for a number of different applications in plant and animal microscopy.

MATERIALS AND METHODS

Sampling and Fixation

Maize inbred lines B73 and Mo17 were grown in growth chambers under long-day light conditions (16 h light/8 h dark). Temperatures within the chambers were maintained at 25°C during the light period and 18°C during the dark period. Inoculation was carried out 21 days after planting. For *C. heterostrophus*, plants were spray-inoculated at the fifth leaf with 5×10^4 spore solution that consisted of *C. heterostrophus* spores suspended in a chilled solution of 0.05% agar and 0.05% Tween 20. The plants were allowed to dry for 30 min and then placed in clear plastic bags for ~16 h overnight, after which the bags were removed. Leaf samples were collected from the fifth leaf at 12, 24, and 48 h postinoculation. For *S. turcica*, the fifth leaf was spray inoculated with a spore suspension consisting of 5×10^4 conidia per milliliter with 0.02% Tween 20. After inoculation, the plants were placed in a mist chamber with >85% humidity overnight. Leaf samples were collected from the fifth leaf at 2, 5, 8, and 10 days postinoculation. The ear leaf of adult plants growing in the field was sampled for image analysis of *C. zeae-maydis*. Debris from previous seasons contained enough natural inoculum that artificial inoculation was not necessary.

Four tissue samples per leaf were excised using a 14-mm^2 punch (www.scrappilyeverafter.com) and placed into 24-well tissue culture plates containing 2 mL of fixative containing 2% glutaraldehyde, 2% paraformaldehyde, and 0.05% Triton X-100 in 1× PBS pH 7.4 (note: use of fresh glutaraldehyde and paraformaldehyde will limit background fluorescence from the fixative). During sampling, plates with fixative were kept on ice. The following procedure was performed at room temperature and used to ensure an even distribution of fixative within the tissue samples and to remove air pockets. Weights (e.g., balls of aluminum foil) were placed over each leaf sample such that it remained submerged in solution (Supporting Information Fig. S1A). Plates were transferred to a bell jar and incubated under vacuum at 30 inHg for 3 h. The weights and fixative solution were discarded, and each well was replenished with 2 mL 1× PBS and a new weight. At this stage in the protocol, samples that float in solution may still contain air pockets and require an additional incubation period under vacuum for optimal downstream processing. Therefore, all samples were incubated under vacuum at 30 inHg for an additional 18 h and then rinsed three times with 1× PBS to remove residual fixative solution. We found that 18 h at 30 inHg to be sufficient (Supporting Information Fig. S1C). Plates were sealed using parafilm and kept at 4°C.

Optical Clearing and Fluorescence Optimization

Six clearing methods were evaluated. For the Sca*l*eP method (Warner et al., 2014), fixed leaf tissue samples were (i) incubated for ~18 h in 0.2 M glycine; (ii) rinsed three times for 5 min in 1× PBS; (iii) incubated for 5 days in a mixture of 1.09 mM Calcofluor White MR2® (CW; Sigma-Aldrich, St. Louis, MO) and 0.026 mM wheat germ agglutinin conjugated to Alexa Fluor® 568 or 594 (WGA-AF568/WGA-AFF594; Thermofisher

Scientific, Carlsbad, CA); (iv) rinsed three times for 5 min in 1× PBS; (v) incubated for 48 h in Sca*l*eP (6 M urea, 30% glycerol, and 0.1% Triton X-100© [v/v/v] in sterile H_2O); and (vi) placed into 20% glycerol (v/v) prior to mounting. The five other clearing methods included the following modifications prior to step (i) above. For methanol + Sca*l*eP, samples were incubated for 48 h in 100% methanol and rinsed three times for 5 min in 1× PBS. For Visikol (Phytosys LLC, Somerville, NJ), samples were incubated for 48 h in Visikol and rinsed three times for 5 min in 1× PBS. For KOH + Sca*l*eP, samples were incubated for 8 h with 10% KOH (w/v) and rinsed three times for 5 min in 1× PBS. For KOH, the Sca*l*eP incubation step was omitted. For KOH + Sca*l*eP without glycine, the glycine incubation step was omitted.

Sample Mounting and Archiving

Usually immediately and no more than 1 day following incubation in 20% glycerol, samples were mounted between two 113 mm × 75 mm × 0.17 mm cover glass slips (cat. no. 70091137B; Live Cell Instruments, Seoul, South Korea), which we refer to as a slide. Each slide included either 12 or 24 samples arranged in a 3 × 4 or 4 × 6 format, respectively. A black and white template was created that was the same size as the base coverslip, using black squares to represent samples with their ideal placement on a slide. With the template underneath the base coverslip, one drop of 20% glycerol was placed in the middle of each black square where samples were then carefully situated on the drop with the adaxial side of the leaf facing upward. Air bubbles that may have occurred between the sample and base coverslip were gently pushed away using forceps. Additional drops of 20% glycerol were added on top of and between samples until the slide was saturated, but not flooded. The top coverslip was cut to a custom size following a template using a diamond scribe. The coverslip had to be large enough to cover the samples but slightly smaller than the base coverslip to allow room for sealing. The top coverslip was placed down gradually from one long edge to the other to minimize the introduction of air bubbles. The edges of the slide were wiped dry and sealed with clear nail polish. Mounted slides were placed in the dark and stored in a refrigerator to maintain fluorescence and sample stability.

Confocal Microscopy

Laser scanning confocal microscopy was conducted on a Zeiss LSM5 DUO (Carl Zeiss, Inc.) using the LIVE line-scanning scanhead. Three objectives were examined including a 5× Fluar with a 0.25 Numerical Aperture (NA), a 10× Plan-Apochromat (0.45 NA), and a 20× Plan-Apochromat (0.8 NA). The 405- and 561-nm laser lines were used to detect CW and WGA-AF594, respectively. Fluorescence emission was collected with a band pass of 415–480 nm for CW and 575–615 nm WGA-AF594, respectively. Tile scans (10 × 10) were collected with a pinhole of 10 μm and gain values between 3 and 5 on the linear charged coupled device camera. Image size was 256 × 256 pixels with 4× binning and 0.5× zoom. *Z*-interval size was 1.2 μm for 150 *z*-slices with a fast Piezo objective nanopositioner (Physik Instrumente, Auburn, MA).

Multiphoton microscopy was conducted on a Zeiss LSM510 NLO or Zeiss LSM880 NLO equipped with a 5W Verdi pumped Mira (Coherent, Inc., Santa Clara, CA) multiphoton tuned to 745 nm. Comparison of single-photon and multiphoton excitation was conducted on a Zeiss LSM780 with a Chameleon Vision multiphoton tuned to 760 nm. The 405- and 561-nm laser lines were used to detect CW and WGA-AF594, respectively. Fluorescence emission was collected with a band pass of 412–482 nm for CW and a BP 569–648 nm for WGA-AF594. The *z*-interval size was 0.400 μm, and image size was 1024 × 1024 pixels. Gain value of the GaAsP detector was 690 for both channels. Laser power was adjusted between 0.3% and 7.5% for the 405-nm laser, 1.8–15% for the 561-nm laser, or 2.8–9% for the 760-nm multiphoton laser through the stack to correct for signal loss through the sample.

3D Image Processing and Rendering

Multiphoton images were deconvolved using Huygens software (Scientific Volume Imaging, Hilversum, Netherlands) and the Classic Maximum Likelihood Estimation algorithm. Images were then imported into Amira 6.0.1 (FEI, Hillsboro, OR) for 3D segmentation, volumetric rendering, and surface rendering.

Cyberinfrastructure

Image processing was performed on a Dell PowerEdge R715 server (2× AMD Opteron 6172 [twelve-core] 2.10 GHz processors; 128 GB RAM). Data management and processing pipelines were developed using modified and custom Visual Basic, Java, Matlab, and Shell scripts (more on these below). The overall workflow for high-speed confocal image data processing included (i) image acquisition (100 confocal image tiles per leaf punch taken across the sample in a 10 × 10 grid with 8% overlap between neighboring tiles in the *XY* plane); (ii) "shade" correction to remove intensity variation; (iii) tiling reconstruction in which the 100 tiles from each leaf sample were stitched together to reconstruct the full leaf punch area in microscopic detail; and (iv) transfer of stitched images to CyVerse-BISQUE for viewing, annotating, and sharing.

Grid-Based Stitching and Image Enhancement

Heterogeneity in the illumination profile of the confocal microscope created light artifacts in each image tile. Prior to computational stitching of image tiles (described below), "shade" corrected image tiles were calculated as follows:

$$\mathbf{C}_{(xy)z} = \alpha * \mathbf{S}_{(xy)z} / \mathbf{P}_{xy;}$$

where *x* and *y* index vertical (row) and horizontal (column) positions, respectively, nested within *z* levels of depth (i.e., *x* and *y* were processed per level of *z*), **C** is a 3D array of intensity values corresponding to a shade-corrected sample tile (i.e., expected image under uniform illumination), **S** is a 3D array of intensity values corresponding to a sample tile, α is a constant that simulates uniform illumination using the maximum intensity pixel value in **P** for α, and **P** is a 2D matrix of intensity values corresponding to the illumination

profile of a reference tile (captured from evenly fluorescent reference Chroma slides). $\mathbf{S}_{(xy)z}/\mathbf{P}_{xy}$ is a measure of the albedo of a sample, and here we have ignored noise that may exist in $\mathbf{S}$.

Accuracy of the reference image is critical for optimal shade correction, and we recommend collecting a reference image for each corresponding band pass in each imaging run (in our case, 12 or 24 samples on a slide were captured in one run and we created one reference tile per band pass to apply shade correction to those images).

Stitching was performed for the high-speed confocal data using Fiji (Schindelin et al., 2012). The source code of the stitching grid plugin proposed by Preibisch et al. (2009; downloaded on December 19, 2013 from https://github.com/fiji/Stitching/tree/master/src/main/java/plugin/) was modified to be server compatible (GUI independent), to improve stitching accuracy and efficiency, and to append metadata to the reconstructed image (https://github.com/drmaize/compvision/tree/master/MMDMS).

Stitching Accuracy. Preibisch et al. (2009) performed local 3D alignment of neighboring tiles using the phase correlation approach. This was followed by a global optimization step to determine the final position of each tile in the stitched image. Global optimization was performed by iteratively ignoring local alignment estimates that were considered to be incorrect, which produced positions that deviated from the mean position of a tile beyond prespecified thresholds (Preibisch et al., 2009). Here, this algorithm was modified to prevent alignment between tiles at different locations in z; at each location along z, phase correlation was applied only to data at the same depth location. This modification prevents errors in z alignment, assuming no z-offsets have occurred when imaging different tiles. Furthermore, translation estimate errors (now, only XY alignments) were minimized by constraining translation between tiles according to the percentage of overlap used to image neighboring tiles (here, 8%).

Stitching Speed. Preibisch et al. (2009) calculated the value for each overlapping pixel in a stitched image as a weighted average, according to the distance of the pixel from the center of each overlapping tile. For each pixel location in the stitched image, rather than determining which tiles contributed to the value at a pixel, we took advantage of our known grid structure and used only those tiles expected to be contributing to the pixel. In our case, this minimized the search space to the nine neighboring tiles instead of all 100 tiles.

For situations in which an inaccurate or no reference tile is available for "shade" correction, a post-stitching shade correction procedure was also developed, using Matlab 2013. In reference to the entire stitched image (rather than an image tile), a shade-corrected image was calculated using the following model:

$$\ln(\mathbf{C}_{(xy)z}) = \ln(\mathbf{S}_{(xy)z}) - \ln(\mathbf{P}_{(.y)z}) + \ln(\mathbf{P}_{(.)z});$$

where $\mathbf{C}$, $\mathbf{S}$, and $\mathbf{P}$ now refer to the entire stitched image. Here, the multiplicative model (from above) was transformed into an additive model to accommodate estimation of the illumination profile via fast Fourier transform (FFT) for constructing the reference for shade correction ($\mathbf{P}$). To estimate this profile, FFT of the natural logarithm of the vector of mean intensities along i of $\mathbf{S}$ was calculated. Furthermore, $\mathbf{S}$ was separated into three sections, such that the shading correction procedure was applied separately to three blocks of rows of the stitched image, which minimized issues associated with potential misalignment along columns (column-wise shade artifacts in stitched images were not perfectly vertical). To approximate $\ln(\mathbf{P}_{(.y)z})$, amplitudes of all frequencies were set to 0 except for the m dominating frequencies 0, n, $2n$, $3n$, . . ., mn (where n is the number of tiles along j), and the inverse Fourier transform was applied. The overall approach for shading correction was similar to the method described by Du and Sun (2009), with the difference being that we approximated the shading effect using sum of sine/cosine functions (taking advantage of the repeating pattern across the stitched image) rather than a low-degree polynomial, and we ignored the additive component of noise. $\mathbf{P}$ and $\mathbf{S}$ were not perfectly aligned due to stitching, and some irregularity in the amount of overlap occurred between adjacent tiles across a stitched image. Therefore, prominent peaks or valleys of $\ln(\mathbf{P}_{(.y)z})$ and $\ln(\mathbf{S}_{(.y)z})$ were identified and aligned by piecewise scaling of $\ln(\mathbf{P}_{(.y)z})$. Finally, the shade-corrected image, $\mathbf{C}$, was obtained by exponentiation.

RESULTS

A Platform for Multiscale Imaging of Multiple Samples

A major challenge of analyzing fungal infection in maize tissue is the large, millimeter-scaled expansion of infection when compared with the small, micrometer-scaled interactions and features, such as penetration by the pathogen into host cells, branching of hyphae during pathogen invasion, and distribution of hyphae resulting from pathogen colonization in different tissue layers. In general, capturing multiple scales of detail in a way that the data can be correlated and analyzed unbiasedly with computational tools is a major challenge in microscopy. Here, we describe the methodologies of a platform designed for semiautomated 3D imaging of plant–fungal interactions. The methodologies include sample fixation, clearing, staining, mounting, confocal imaging, computational stitching of images, and image analysis (Fig. 1). We have optimized these methods to create an efficient workflow for multiscale 3D analysis of multiple organisms or structures within a specimen sampled from across a time course (4D). Each method within the platform has the potential to be co-opted for a variety of plant imaging applications and, therefore, can be broadly used by the research community. We describe below how these methods were developed and combined to study fungal pathogenesis on maize.

Optimized Fixation of Maize Leaf Tissue for Staining and Long-Term Sample Preservation

The need for a clearing technique for maize leaf tissue arose when attempting to image formaldehyde-fixed tissue stained with fluorescent dyes; we saw no

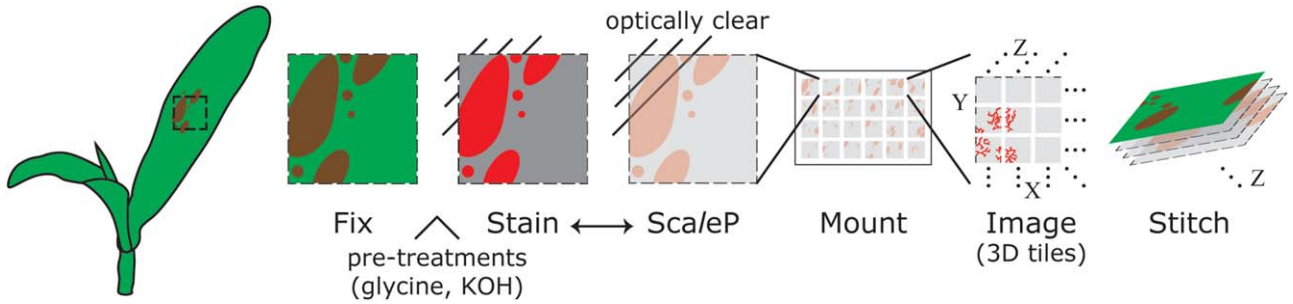

Fig. 1. Workflow for 3D confocal microscopy of macroscopic samples. The figure cartoons a maize plant with lesions induced by pathogen infection. A section of the leaf tissue is excised, fixed under vacuum (typically in a 12- or 24-well plate; e.g., Supporting Information Fig. S1), and appropriately pretreated for subsequent processing. Next, samples are fluorescently stained with dyes that distinguish specimens or structures of interest (in our case, CW was used to stain plant cell walls and WGA was used to stain fungal hyphae). Samples are then cleared with Sca*l*eP. The steps for staining and clearing may be applied in either order (although this has not been thoroughly tested). Processed samples are mounted in a multisample format appropriate for tiled imaging of multiple samples using a motorized microscope stage. Partially overlapping tiles within each sample are imaged across a macroscopic sample space. A file naming convention that serves to index the *XY* location of each image tile is leveraged for stitching the tiles into their original sample structure. [Color figure can be viewed in the online issue, which is available at wileyonlinelibrary.com.]

fungal infection despite the presence of clear lesions visible by eye. After a close examination by differential interference contrast, we determined that there was indeed fungal infection, but it was not detectable by fluorescence-based methods due to poor dye penetration and imaging depth. To overcome these problems, we first optimized conditions for aldehyde-based fixation. Our initial method of 3 h of vacuum infiltration did not result in complete exchange of the air inside the leaves with fixative (Supporting Information Fig. S1), and air pockets can result in uneven staining. However, after 18 h of vacuum infiltration, all air pockets were removed. In the optimized procedure, a combination of 2% paraformaldehyde for more rapid penetration and initial fixation with 2% glutaraldehyde for crosslinking and long-term sample stability was used. Samples submerged in fixative solution were initially placed under vacuum for 3 h and then transferred to PBS and placed under vacuum overnight (~18 h) to completely remove air bubbles. Samples fixed, stained, cleared, and mounted by this procedure have been stable (and successfully reimaged) for over 2 years at 4°C, suggesting that the samples have been properly fixed. For *Nicotiana benthamiana* tissue, pulling and releasing a vacuum in a 10-mL syringe three times is a more efficient rapid method for a small number of samples. We used that method previously to fix and preserve citrine fluorescent protein fluorescence (Warner et al., 2014).

All of the staining and clearing steps (below) were performed in 24-well dishes, and the samples were mounted between large cover glasses for automated multisample imaging. To match the sample processing layout, the samples were mounted in 12 (half a plate) or 24 (full plate) sample formats. Initially, we used a Chamlide magnetic system (Live Cell Instruments) and VALAP (vasoline lanolin paraffin) on a hot plate to rapidly seal the samples. However, because of the flexibility of the large cover glasses, the seal was easily broken. Although slower and more tedious, nail polish sealing was more durable for long-term storage and repeated confocal imaging (Supporting Information Fig. S2).

Development of a Clearing Method That Improves Imaging Depth

The other main barrier for imaging was the opacity of leaf tissue (Fig. 2). The problem is a result of pigments such as chlorophyll and the natural light scattering and refracting properties of cell walls. We were not authorized to use chloral hydrate, and therefore, we tested a number of unrestricted chemical compounds for clearing. This led to the development of a modified form of the clearing reagent *Scal*e (Hama et al., 2011), which we call *Scal*e for Plants or Sca*l*eP (Warner et al., 2014). Warner et al. (2014) demonstrated that Sca*l*eP alone cleared nodule tissue quite well; however, Sca*l*eP alone did not completely clear maize leaves, and therefore, a combination of KOH and Sca*l*eP was required (Fig. 2A). We investigated alternative pretreatments used previously to clear plant tissue: KOH (control), methanol, and Visikol (Obrien, 1974; Talbot and White, 2013; Villani et al., 2013). Both pretreatment with methanol and Visikol resulted in limited enhancement of clearing and imaging depth. However, pretreatment with KOH consistently enhanced clearing and the ability to image through the entire thickness of a maize leaf (the average leaf thickness measured on 72 stitched images was ~90 μm), allowing for the visualization of structures in the epidermal layers, mesophyll cells, bundle sheath cells, vascular bundles, and stomata (Fig. 2B), and hyphae stained with WGA conjugated to Alexa Fluor® 568 (WGA-AF568) could be detected deep within the leaf tissue. Furthermore, the combination resulted in a remarkable increase in CW staining. An image taken with the same acquisition settings used to image all other treatments has been provided for comparison (Figs. 2B and 3). Other treatments with 2,2′-thiodiethanol, ethanol, acetic acid, and acetone were attempted with limited investigation or success. A final modification to the protocol was an initial treatment with 0.2 M glycine to quench green to red autofluorescence associated with glutaraldehyde fixation. This treatment vastly improved signal-to-background of the hyphae labeled with the red fluorescent stain WGA-AF568 (Fig. 2C).

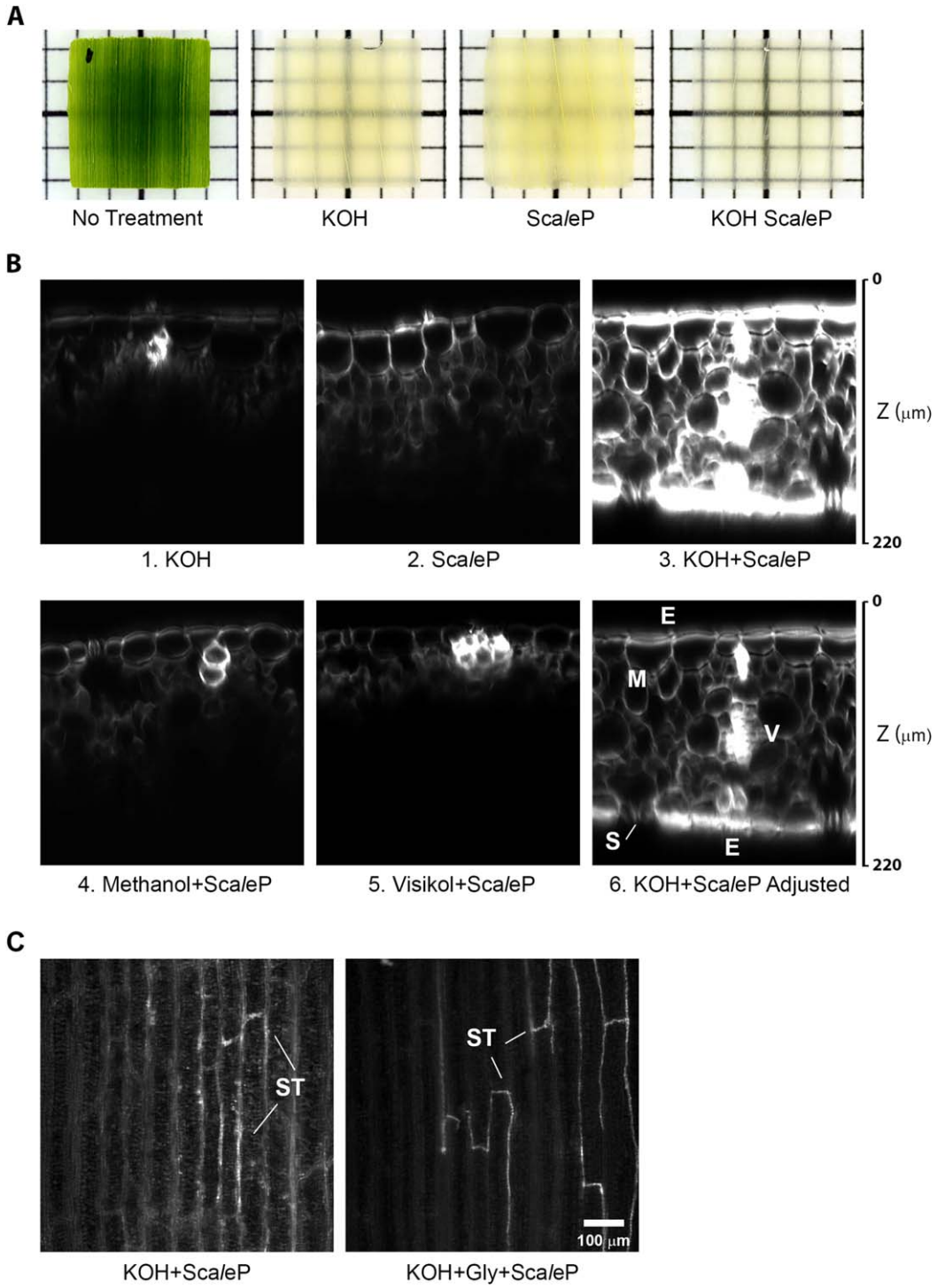

Fig. 2. Optical clearing methods applied to maize leaf tissue. **A**: Digital camera images of 14 mm × 14 mm uninfected leaf punches. From left to right: leaf punch in buffer (1× PBS); 8-h treatment with KOH; 48-h treatment with Sca*l*eP; and 8-h treatment with KOH followed by 48-h treatment of Sca*l*eP. **B**: Multiphoton cross-sections of cell walls stained with Calcofluor White MR depicting depth of clarity in uninfected samples. The first five panels were taken with the same settings. The resulting increase in tissue transparency from the successful combination of Sca*l*eP and KOH led to image saturation at the same settings. Therefore, the sixth panel shows the same cross-section using optimized acquisition settings. Various features of the tissue can be resolved, including the epidermis (E), mesophyll (M), vascular bundle (V), and stomata (S). **C**: Eighteen-hour treatment of 0.2 M glycine shows a great reduction in autofluorescence and clearer detection of *S. turcica* stained with WGA-AF594 in vascular tissue (right) when compared with no treatment (left). Confocal images of two samples infected with *S. turcica* (ST) taken with the same settings. Scale bar = 100 μm. [Color figure can be viewed in the online issue, which is available at wileyonlinelibrary.com.]

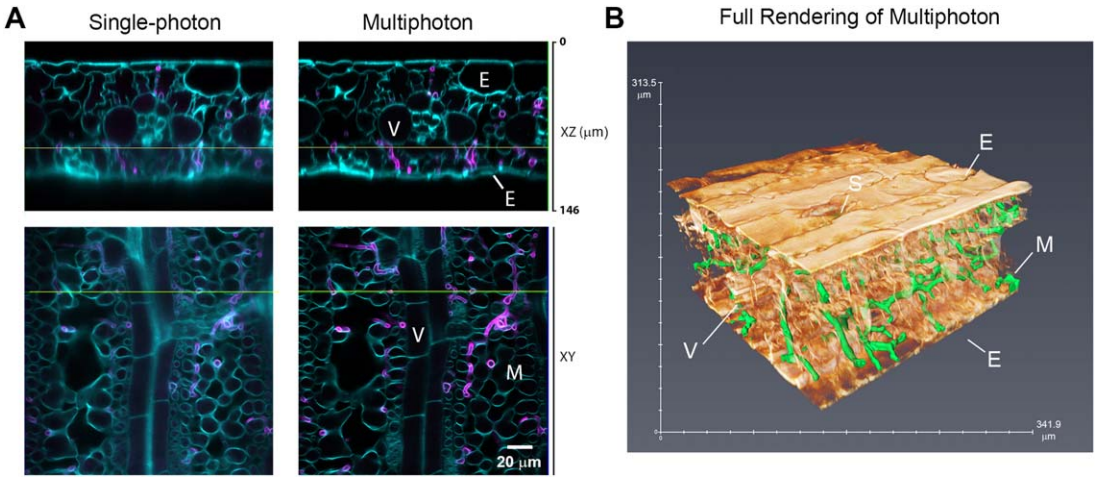

Fig. 3. Comparison of single-photon and multiphoton confocal microscopy. **A**: Cell walls were stained with Calcofluor White (cyan) and fungi with WGA-AF594 (magenta). Yellow line at ~90 μm in cross-section shows where an *XY* slice comparison was captured. Resolution differences become obvious deeper into the sample, particularly with the lower epidermis (E). Vascular bundles (V) and mesophyll (M) were easily identified in the multiphoton dataset, and hyphae from *C. heterostrophus* infection was more clearly detectable (magenta). The yellow lines in *XY* slice corresponds to the location of the *XZ* cross-sections. Scale bar = 20 μm. **B**: 3D voltex rendering of the multiphoton data in (A) showing the leaf (amber) and segmented surface rendering of *C. heterostrophus* (green). One stoma (S) is visible on the surface, and the fungal network was detected throughout the mesophyll and near vasculature. Multiphoton data were deconvolved (Huygens Pro) prior to rendering in Amira 6.0.1. [Color figure can be viewed in the online issue, which is available at wileyonlinelibrary.com.]

A Stain Combination for Plant Tissue Structure and Fungal Detection

Although CW stains both plant and fungal cell walls, it was nearly impossible to distinguish between the plant and fungi based on structure alone. Hence, it was essential for us to find another stain that was specific to fungi. We tested a number of dyes including aniline blue, safranin, ruthenium red, solophenyl flavine, propidium iodide, trypan blue with lactophenol (data not shown), and WGA that have all been reported to successfully stain fungi (Chung et al., 2010; Hood and Shew, 1996; Howard, 2001; Knight and Sutherland, 2011). WGA provided the best specificity, which was surprising as it reportedly binds any sialic acid or *N*-acetylglucosaminyl residues (Monsigny et al., 1980). As it is also widely used to stain the plasma membrane, it was quite unexpected that it did not stain the plant tissue. Interestingly, WGA has been used previously to detect fungi in resin embedded and sectioned samples using standard electron microscopy protocols (Meyberg, 1988; Rath et al., 2013). Another significant advantage of using WGA over other dyes is that it can be conjugated to dyes with varying fluorescent properties. As it is the most widely used lectin in microscopy, blue, green, red, and far-red dye conjugates are readily available. WGA-conjugated Alexa Fluor® 568 (WGA-AF568) or Alexa Fluor® 594 (WGA-AF594) was chosen for our study because their emission spectra are easily separated on most fluorescent microscopes, including laser scanning confocal microscopes. Furthermore, a common multiphoton excitation wavelength (745–760 nm) can excite both CW and WGA-AF568 or WGA AF594 (Fig. 3). Because of the superior clearing, we were able to obtain excellent image quality with a 40× C-Apochromat (NA 1.2) water objective with single-photon excitation (Fig. 3A). However, multiphoton microscopy resulted in less out of focus light and scattering, and higher image quality when compared with single-photon confocal microscopy and was superior for 3D segmentation and rendering (Fig. 3B). Multiphoton microscopy is the modality of choice; however, high-quality data can still be collected with the more widely available single-photon confocal microscopes.

Optimized Large-Scale 3D Imaging

Medium-to-large-scale imaging is often a balance between resolution and speed. To determine what *X*, *Y*, and *Z* resolution was required for our study, we examined the resolution of three microscope objectives with different magnifications and numerical apertures. We chose a 5× Fluar (0.25 NA), a 10× Plan-Apochromat (0.45 NA), and a 20× Plan-Apochromat (0.8 NA) for analysis. Lower magnifications allowed faster imaging of larger areas at the expense of resolution. All objectives resolved hyphal networks and plant structures, such as guard cells, in *XY* (Fig. 4A). For analyses that do not require 3D information, 10× magnification seemed to be an excellent compromise between field of view and resolution. For our study, however, we wanted to capture the 3D distribution of plant–pathogen interactions. The examination of *XZ* cross-sections through hyphae with the three objectives showed that the 20× Plan-Apochromat (NA 0.8) was required to resolve the location of hyphae in 3D and to resolve both the adaxial and abaxial surfaces of the leaf. Furthermore, individual hyphal strands could be resolved in *Z* with 20× but not the 10× objective (Figs. 4B and 4C). The analysis of fungal width distributions from 20× data (data not shown) indicated that a pixel resolution of ~1.2 μm can resolve the majority of hyphae; however, the sparseness of hyphal growth may permit

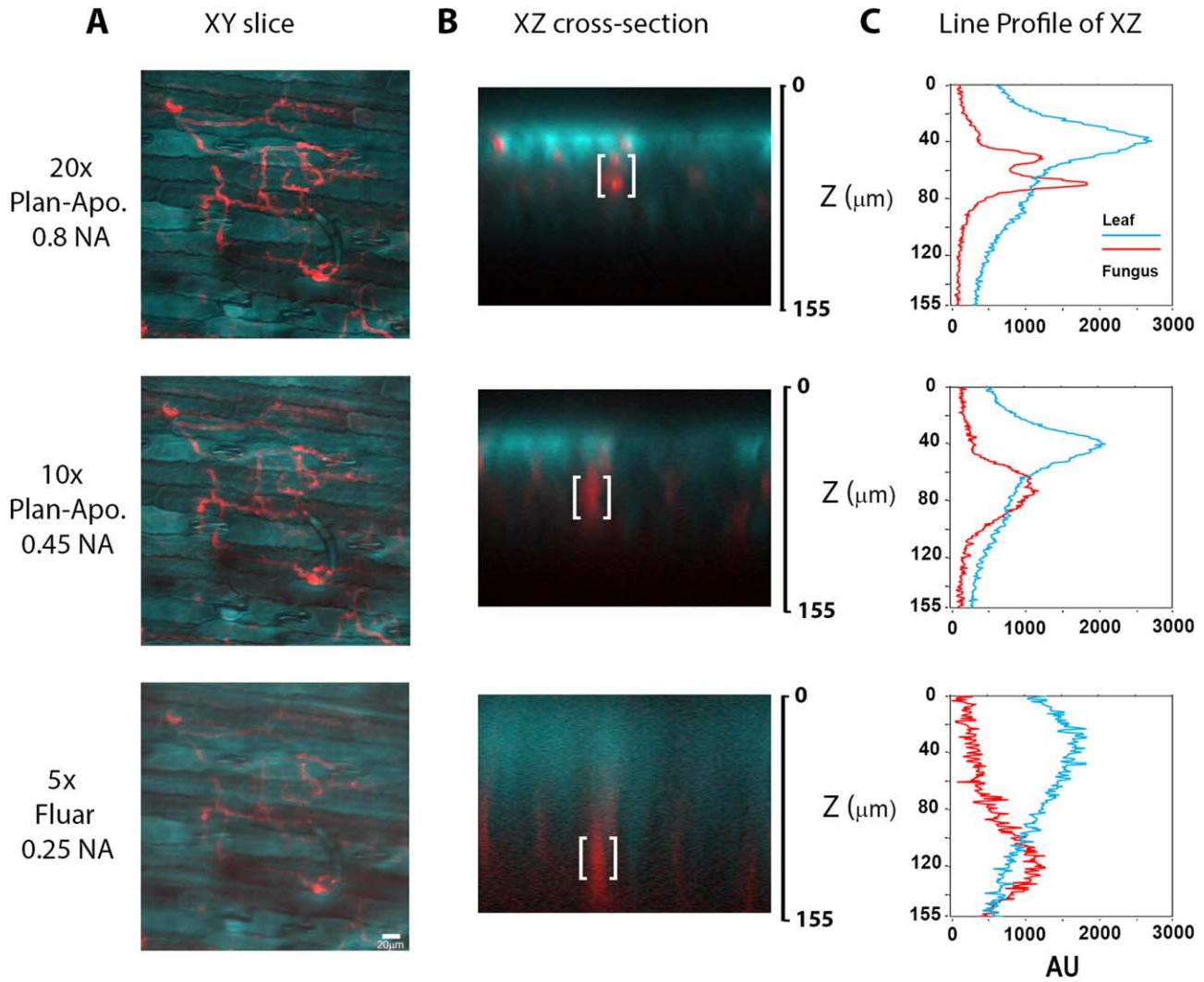

Fig. 4. Resolving features of *C. heterostrophus* in cross-section. **A**: Cell walls were stained with Calcofluor White (cyan) and fungi with WGA-AF594 (red). The same sample was imaged at a depth of 155 μm using 20× Plan-Apochromat 0.8 NA, 10× Plan-Apochromat 0.45 NA, and 5× Fluar 0.25 NA. The zoom for 10× and 5× objectives were adjusted to match that of 20×. Maximum intensity projections (MIP) of the fungal channel (red) reveals there is minimal difference in *XY* fungal detection (red) using 20× and 10× objectives. Image quality decreased with 5×. **B**: A cross-section taken at the same point shows the dramatic difference in resolution between each objective. **C**: A signal profile of the bracketed area in 20× shows two peaks, distinguishing that there are two separate hyphae at different levels of deepness. The profiles of the same area imaged with both the 10× and 5× objective show that the signal between those two strands could not be separated. Profiles of the leaf channel for both 20× and 10× show clear peaks that correspond with the upper leaf surface. [Color figure can be viewed in the online issue, which is available at wileyonlinelibrary.com.]

imaging at a lower resolution, particularly for the analysis of hyphae at the 2D *XY*-millimeter scale.

The requirement of a 20× Plan-Apochromat (NA 0.8) for axial resolution meant that a large grid of tiled images was required to cover a sufficiently large area of the sample. The central region of each 14-mm^2 leaf sample was captured in a 10 × 10 grid of image tiles, representing a leaf area of 6 mm^2 (Fig. 5 and Supporting Information Fig. S5). Each tile contained 150 *z*-slices to capture the full depth and contours of the leaf. To collect this large amount of data in a short period of time, we chose a line-scanning confocal microscope (Zeiss LSM5 DUO) that can operate at up to 120 frames per second, full frame. The system was fitted with a high-speed Piezo motor objective positioner, a requirement for fast imaging of 150 *z*-slices. For each tissue sample, CW (plant) and WGA (fungal) channels were imaged across the 10 × 10 grid comprising 30,000 images that could be collected in ~30 min. Although we used a high-speed, line scanning confocal microscope for image acquisition, it is possible that other fast 3D imaging systems can be used; this includes resonant point scanning confocal microscopy, spinning disk confocal microscopy, wide-field fluorescence microscopy with deconvolution, and fluorescent slide scanning systems.

A Modified Tile Stitching Algorithm for Macroscale Microimaging Studies

Each 10 × 10 tile dataset with 150 *z* stacks per tile were stitched into a single, combined image for the analysis of features across millimeters of leaf tissue.

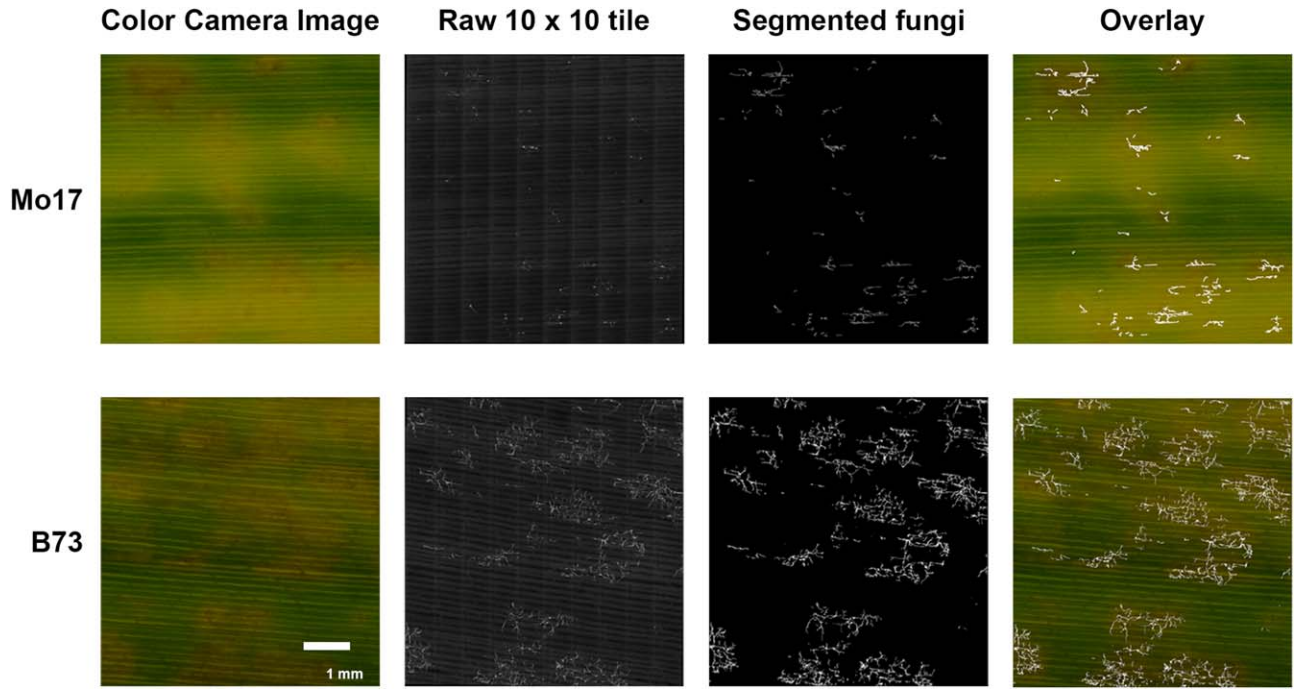

Fig. 5. Macroscopic microscopy. The 14-mm^2 leaf punches from quantitatively resistant Mo17 (top row) and susceptible B73 (bottom row) were collected from plants 48 h postinfection with *C. heterostrophus*. Each sample was photographed before clearing with a Nikon camera (Column 1). Fungal hyphae was labeled with WGAAF594, and confocal microscopy *Z*-stacks of 150 slices were collected in a 10 $\times$ 10 array of the 6 mm^2 center portion of the leaf (Column 2). The 100 *Z*-stacks of images were reconstructed using our modified ImageJ program and maximum intensity projections were created. Brightness and contrast settings of the Mo17 image were adjusted to match B73. Images were segmented by thresholding (Column 3) and overlaid on the color camera picture (Column 4). Scale bar = 1 mm. [Color figure can be viewed in the online issue, which is available at wileyonlinelibrary.com.]

An Excel-based macro user interface with associated scripts was developed for stitching on a high-performance computer cluster. The underlying stitching scripts included modifications or extensions to those developed by Preibisch et al. (2009). The method proposed by Preibisch et al. (2009) represents a generalizable approach to stitching. Given our knowledge of the *XY* location of each image tile and under the assumption that the microscope captures images at the same *Z*-plane across the *XY* area imaged, the accuracy and speed of this method could be improved by adding constraints on the translation parameters estimated for aligning adjacent tiles.

The default stitching method, relying on phase correlation to identify and reposition corresponding *Z*-data across *XY* into the same *Z*-plane, resulted in numerous misalignments of our data, and not a single tile dataset was accurately stitched (>24 tile datasets tested; Supporting Information Table S1). We speculate that this is partially related to difficulties in aligning *Z*-slices that, in our data, contain little information due to imaging empty areas from above the top and below the bottom surfaces of the sample. Nevertheless, we were interested in preserving the sample topography, and thus, we restricted *Z*-alignments to the original *Z*-planes of the data which resulted in error-free alignments (determined by manual inspection of stitched images).

For higher throughput applications, the speed of stitching could also be a limitation. By restricting the stitching search space to tiles known to be adjoining, the time of stitching 100 tiles was increased by $\sim$4$\times$ (Supporting Information Fig. S3).

Stitched images exhibited shade artifacts that were readily visible along the vertical edges of each tile (Supporting Information Fig. S4). To normalize the light-intensity profile across stitched images, prestitching and post-stitching shade correction methods were applied to the data. Both methods produced similar results in terms of normalization of the signal profile and in terms of the appearance of an edge map of features on the epidermal surface (Supporting Information Fig. S4). In principle, prestitch shade correction is optimal because it captures specific *XY* pixel correction; however, this depends on the accuracy of the reference file used for shade correction. Post-stitch shade correction is performed without the need for a reference file and the produced results were highly similar to prestitch shade correction with our data; however, here and in other instances, it could be less accurate than prestitch shade correction.

Stitched images serve two main purposes in our application. The first is to extract quantifiable fungal and plant features from large 3D data sets. We are currently working on algorithms for quantifying spores, germination, hyphal width, hyphal length, and hyphal area, and relationships to plant features, such as stomata and vascular tissue. The second is to identify and target specific areas for multiphoton microscopy, which provides data with a better signal-to-noise ratio and apparent resolution at the expense of speed.

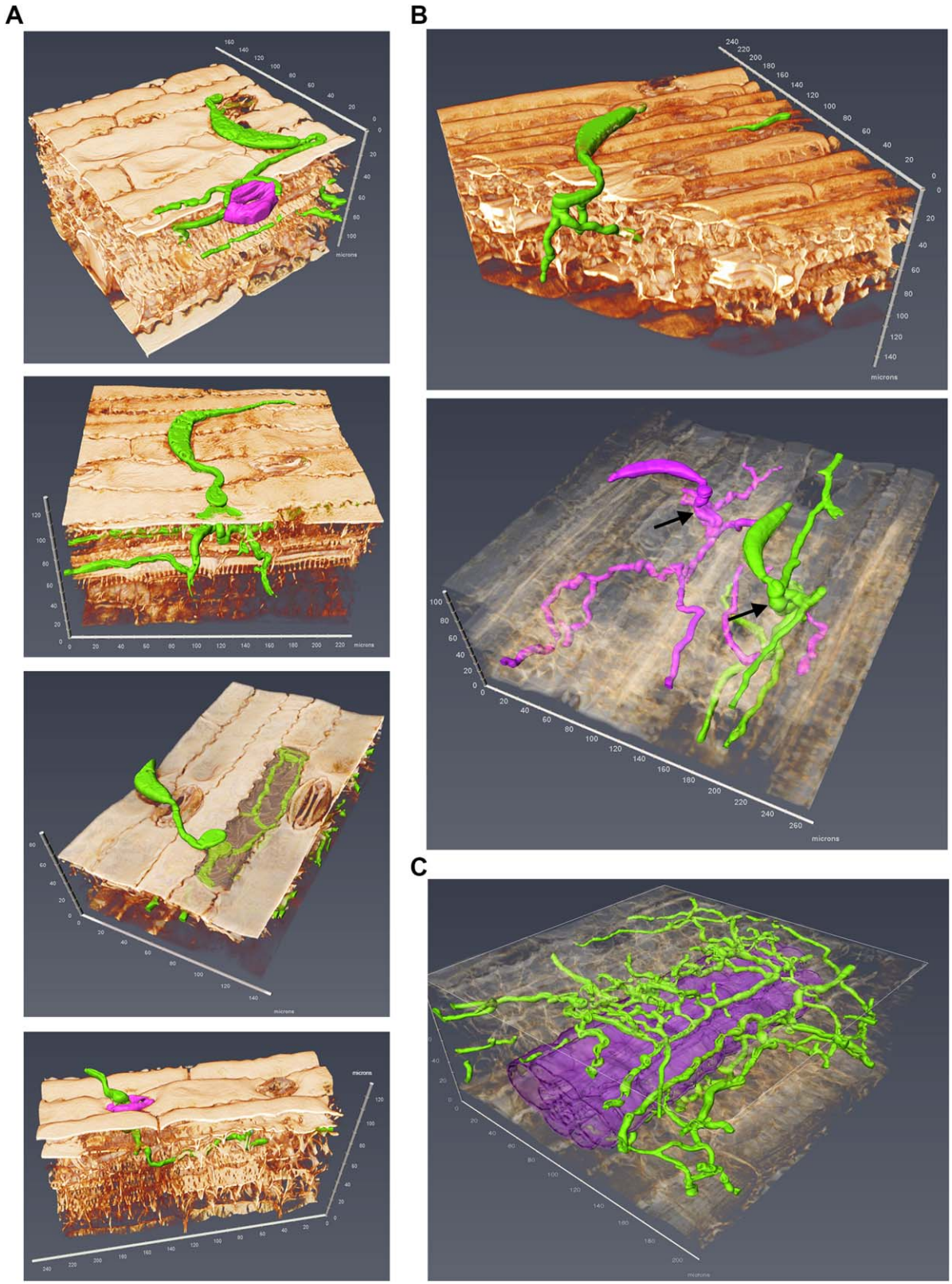

Fig. 6. Pathogenesis of *C. heterostrophus* rendered in 3D. **A**: Cell walls were stained with Calcofluor White (amber) and fungi with WGA-AF594. Three different types of fungal (green) penetration events were observed. The first two panels show the more commonly reported event types; between a guard cell (pink) and subsidiary cell and between two epidermal cells. Intracellular penetration takes place in the third panel where hyphae can be seen occupying space inside an epidermal cell. The final panel shows successful invasion of fungus (green) through the opening of a guard cell (pink). **B**: Branching in *C. heterostrophus* is shown in the first panel as a simple split in a strand of hyphae shortly after penetrating between two epidermal cells. The second panel has two networks of hyphae (green and magenta) showing the formation of a bulbous structure before branching resulting in more than two hyphal strands. See Supporting Information Movie S1. **C**: An example of the distribution of *C. heterostrophus* throughout a leaf sample. Fungus (green) can be seen shrouding around the vascular bundle (purple). See Supporting Information Movie S2. [Color figure can be viewed in the online issue, which is available at wileyonlinelibrary.com.]

High-Resolution Analysis of Fungal Infection by Multiphoton Microscopy

Multiphoton microscopy is significantly slower than line-scanning confocal microscopy, but for higher resolution deep tissue imaging, it is far superior. Our workflow uses multiphoton microscopy to detect and characterize features of pathogenesis. This information can subsequently be used to verify and improve the analysis of large (lower resolution) 3D datasets.

An example of how information is correlated between large-scale tiled images and high-resolution multiphoton microscopy is the characterization of different types of penetration by *C. heterostrophus*. We observed three types of penetration in between cells, through stomata, and intracellular penetration (Fig. 6A). Penetration through the opening of guard cells occurred less often than penetration between two epidermal cells or between a stomata and a subsidiary cell. This may be due to the limited availability of stomata versus the abundant amount of intercellular opportunities. However, many penetrations are preceded by lengthy growth on the surface of the leaf. This suggests that intercellular penetration is the preferred method of entry. Both intercellular and stomatal infections are generally successful events leading to extended hyphal networks deep into the leaf tissue. In comparison, intracellular penetration events appear to remain contained within the cell it penetrated. We are currently developing algorithms to quantify these three types of penetration at the macroscopic scale.

Branching in *C. heterostrophus* is another quantifiable feature in pathogenesis (Fig. 6B; see Supporting Information Movie S1). Often branches are simple bifurcations of hyphae. Simple branches are seen all throughout a given fungal network and sometimes as a feature of surface growth. More complicated branching has been observed where one or more strands appear to originate from a bulbous structure; the fungus usually forms shortly following penetration between two epidermal cells. This provides information on features of the network to be considered in quantifying macroscale hyphal networks in planta.

Finally, the increased resolution provided by multiphoton microscopy allows for detailed analysis of fungal distribution (Fig. 6C; see Supporting Information Movie S2). We have observed that shrouding of hyphae around vascular bundles is common in *C. heterostrophus* infections; the fungus can be seen wrapping around bundles and growing in their grooves. Large fungal networks near bundles grow in any direction in the space between the small cells surrounding bundles. These intricacies might otherwise go unnoticed in single-photon microscopy.

DISCUSSION

Investigation of microscopic events underlying macroscopic phenotypic variation of biological samples is a complex process with many inherent challenges. Here, we have created and optimized a platform to allow for the characterization and quantification of plant pathogenesis *C. heterostrophus* on maize. We also show that it can be applied without modification for and *S. turcica* and *C. zeae-maydis* on maize. Tissue clearing and staining procedures for the visualization of fungal infection within leaf tissue using conventional and fluorescence microscopy in 2D have been established (Chung et al., 2010; Knight and Sutherland, 2011). Two-dimensional analysis of fungal infection adeptly captures the expansion of hyphal growth but misses pertinent 3D information including penetration, invasion, and localization that occurs at the tissue, cellular, and subcellular level. Our method captures both the 2D expansion of fungal growth at the millimeter scale and the 3D distribution in tissues and cells at the micrometer scale. It is dependent on the sufficiently fixed, cleared, and stained tissue combined with high-speed 3D imaging and computational solutions for data management and image analysis.

Our clearing method was briefly described previously for maize leaf tissue (Warner et al., 2014). In this study, we provide a more in-depth description of modifications to the Sca*l*e protocol that makes Sca*l*eP uniquely suited to clearing plant tissue. An important step, at least for maize leaf tissue, is the KOH treatment that possibly increases clearing by removing the cuticle and macerating the cell wall (Bevege, 1968). Incubating samples too long in KOH caused the tissue to become fragile, possibly distorting cellular structures. The KOH treatment was optimized for juvenile maize leaves, but may need to be altered for older tissue or different plant species. Furthermore, glutaraldehyde fixation is required for long-term storage, and a glycine treatment is required to quench glutaraldehyde autofluorescence, which was essential for distinguishing fungal structures. It must be noted that both KOH treatment and glutaraldehyde fixation may be detrimental to fluorescent protein detection, and the protocol described here should not be used for visualizing green fluorescent proteins; the protocol described in Warner et al. (2014) using paraformaldehyde without KOH or ClearSee (Kurihara et al., 2015) should be used instead. Kurihara et al. (2015) indicated that Sca*l*eP did not clear Arabidopsis leaf tissue within 3 days. To clarify, we note here that longer incubation times are often required for Sca*l*eP-based clearing up to as much as 3 weeks without a KOH pretreatment. For our tissue type, Sca*l*eP provided better clearing than ClearSee (data not shown), suggesting that similar to mammalian tissue clearing approaches, different methods will provide superior clearing for specific applications.

Our future direction is focused on extracting biologically pertinent features using automated algorithms to quantitatively characterize pathogenesis and to differentiate how different genotypes and specific regions of a genome function in limiting pathogenesis and conditioning disease resistance. Currently, we are developing methods for analyzing fungal characteristics, including the number of germinating spores, penetration location, the total hyphal volume, branching patterns, and width across time courses of infection. CW staining of cell walls continues to provide a wealth of plant features to identify and quantify during fungal infection, such as the abaxial and adaxial surfaces, stomata, and tissue types such as the epidermal, mesophyll, and vascular tissue; we are in the process of developing algorithms to detect these plant features to characterize the fungal–plant interactions over time in 3D. We are also investigating if other histological

fluorescent stains are compatible with the Sca*l*eP method to provide information on physiological and biochemical responses to infection.

Correlative microscopic data collection on macroscopic specimens facilitated through semiautomated imaging platforms and computational tools for analysis will be transformative in the characterization of microscopic phenotypes underlying whole plant resistance. The ability to quantify multiple features of plant–pathogen interactions in less time than manual scanning will limit biases and allow future experiments to examine the large sample sizes necessary for population and comparative biological investigation. Although this system has been developed using two specific pathosystems, modifications to the sample preparation portion of this method are easily adaptable and may work for a variety of other plants and pathogens, with some of this potential already demonstrated by Warner et al. (2014) and extended here. We foresee these 3D imaging and digitization procedures to be widely applicable in various plant microscopy investigations where observation and correlation of microscopic and macroscopic features throughout the whole sample is required.

ACKNOWLEDGMENTS

The authors thank Tyr Wiesner-Hanks from the Nelson Laboratory for *Setosphaeria turcica* infected maize samples and Tim Chaya for assistance with multiphoton microscopy. Access to microscopes was made possible by S10 RR027273, S10 OD016361, and Delaware INBRE (P20 GM103446).

REFERENCES

Bevege DI. 1968. A rapid technique for clearing tannins and staining intact roots for detection of Mycorrhizas caused by Endogone spp. and some records of infection in Australasian plants. Trans Br Mycol Soc 51:808–810.

Buda GJ, Isaacson T, Matas AJ, Paolillo DJ, Rose JKC. 2009. Three-dimensional imaging of plant cuticle architecture using confocal scanning laser microscopy. Plant J 60:378–385.

Chung C-L, Longfellow JM, Walsh EK, Kerdieh Z, Van Esbroeck G, Balint-Kurti P, Nelson RJ. 2010. Resistance loci affecting distinct stages of fungal pathogenesis: Use of introgression lines for QTL mapping and characterization in the maize—*Setosphaeria turcica* pathosystem. BMC Plant Biol 10:103.

Du C-J, Sun D-W. 2009. Retrospective shading correction of confocal laser scanning microscopy beef images for three-dimensional visualization. Food Bioprocess Technol 2:167–176.

Hama H, Kurokawa H, Kawano H, Ando R, Shimogori T, Noda H, Fukami K, Sakaue-Sawano A, Miyawaki A. 2011. Scale: A chemical approach for fluorescence imaging and reconstruction of transparent mouse brain. Nat Neurosci 14:1481–1488.

Hood ME, Shew HD. 1996. Applications of KOH-aniline blue fluorescence in the study of plant–fungal interactions. Phytopathology 86: 704–708.

Howard RJ. 2001. Cytology of fungal pathogens and plant–host interactions. Curr Opin Microbiol 4:365–373.

Knight NL, Sutherland MW. 2011. A rapid differential staining technique for *Fusarium pseudograminearum* in cereal tissues during crown rot infections. Plant Pathol 60:1140–1143.

Kurihara D, Mizuta Y, Sato Y, Higashiyama T. 2015. ClearSee: A rapid optical clearing reagent for whole-plant fluorescence imaging. Development 142:4168–4179.

Meyberg M. 1988. Selective staining of fungal hyphae in parasitic and symbiotic plant–fungus associations. Histochemistry 88:197–199.

Monsigny M, Roche AC, Sene C, Maget-Dana R, Delmotte F. 1980. Sugar–lectin interactions: How does wheat-germ agglutinin bind sialoglycoconjugates? Eur J Biochem 104:147–153.

Obrien P. 1974. Autoclaving as an aid in the clearing of plant specimens. Stain Technol 40:40–41.

Palmer WM, Martin AP, Flynn JR, Reed SL, White RG, Furbank RT, Grof CPL. 2015. PEA-CLARITY: 3D molecular imaging of whole plant organs. Sci Rep 5:13492.

Preibisch S, Saalfeld S, Tomancak P. 2009. Globally optimal stitching of tiled 3D microscopic image acquisitions. Bioinformatics 25:1463–1465.

Rath M, Grolig F, Haueisen J, Imhof S. 2013. Combining microtomy and confocal laser scanning microscopy for structural analyses of plant-fungus associations. Mycorrhiza 24:239–300.

Schindelin J, Arganda-Carreras I, Frise E, Kaynig V, Longair M, Pietzsch T, Preibisch S, Rueden C, Saalfeld S, Schmid B, Tinevez J-Y, White DJ, Hartenstein V, Eliceiri K, Tomancak P, Cardona A. 2012. Fiji: An open-source platform for biological-image analysis. Nat Methods 9:676–682.

Sørensen CK, Justesen AF, Hovmøller MS. 2012. 3-D imaging of temporal and spatial development of *Puccinia striiformis* haustoria in wheat. Mycologia 104:1381–1389.

Talbot MJ, White RG. 2013. Cell surface and cell outline imaging in plant tissues using the backscattered electron detector in a variable pressure scanning electron microscope. Plant Methods 9:40.

Villani TS, Koroch AR, Simon JE. 2013. An improved clearing and mounting solution to replace chloral hydrate in microscopic applications. Appl Plant Sci 1:1300016.

Warner CA, Biedrzycki ML, Jacobs SS, Wisser RJ, Caplan JL, Sherrier DJ. 2014. An optical clearing technique for plant tissues allowing deep imaging and compatible with fluorescence microscopy. Plant Physiol 166:1684–1687.

Wuyts N, Palauqui J-C, Conejero G, Verdeil J-l, Granier C, Massonnet C. 2010. Open access high-contrast three-dimensional imaging of the Arabidopsis leaf enables the analysis of cell dimensions in the epidermis and mesophyll. Plant Methods 6:14.